Nanoscale

PAPER

View Article Online
View Journal | View Issue

Check for updates

Cite this: *Nanoscale*, 2025, **17**, 16796

Role of nitrogen and oxygen in the nucleation and growth of silver nanoparticles in gas-phase synthesis†

Salomé Trillot,[a] Patrizio Benzo, *[a] Sophie Barre,[a] Nathalie Tarrat, [a] Magali Benoit,[a] Kremena Makasheva [b] and Caroline Bonafos *[a]

Received 15th April 2025,
Accepted 23rd June 2025

DOI: 10.1039/d5nr01526j

rsc.li/nanoscale

In this study, we synthesized silver nanoparticles (AgNPs) in the gas phase and explored the influence of a small amount of reactive gases on their structural properties. Through a combined approach of transmission electron microscopy (TEM) with atomic resolution and *in situ* optical emission spectroscopy, we investigated the nucleation mechanisms of silver in the gas phase. Our findings put forward the ion-induced nucleation as mechanisms playing a pivotal role in the significant increase in AgNP surface density observed upon the introduction of a small amount of oxygen (below 0.5%). These results provide key insights into the impact of reactive gases on nanoparticles formation and underline the mechanism driving their nucleation in plasma environments.

Open Access Article. Published on 25 June 2025. Downloaded on 2/17/2026 6:44:42 PM.
This article is licensed under a Creative Commons Attribution 3.0 Unported Licence.

1. Introduction

Noble metals such as gold, silver, and copper exhibit exceptional optical and plasmonic properties.[1–3] At the nanometric scale, these metallic nanoparticles exhibit a characteristic localized surface plasmon resonance (LSPR), resulting from the collective oscillations of conduction electrons interacting with light, which largely increased the efficacy of diverse technological applications in photothermal therapy,[4,5] photovoltaics,[6,7] and photocatalysis.[8–10] Along with its optical properties, silver has been recognized since ancient times also for its antibacterial properties, primarily due to the bactericidal action of silver ions (Ag^+), which exert a complex effect within the cell.[11] Silver nanoparticles (AgNPs), commonly referred to as "nano-silver", have recently gained prominence as effective antimicrobial/antibiofilm agents.[12,13] This effectiveness is attributed to their high surface-to-volume ratio.[14,15] Additionally, AgNPs have the advantage of continuously releasing a significant concentration of ions over an extended period.[16,17] However, further studies are needed to assess the biocompatibility and potential cytotoxicity of AgNPs across various systems, including the skin, eyes, kidneys, respiratory, hepatobiliary, immune, and reproductive systems.[18] Since the biocidal activity of AgNPs is usually considered in terms of a dose/contact time pair, it is strongly justified to precisely control the released Ag^+ amount given the potential human and environmental risks. To that end, a simultaneous control of the size and the surface density of the synthesized AgNPs is a good strategy, however presenting a challenge due to the correlation between these two parameters.

AgNPs have been successfully synthesized through both chemical[19,20] and physical methods.[21–24] While the chemical methods are commonly employed due to their efficiency and cost-effectiveness, they can introduce impurities from reactants and stabilizing agents. In contrast, physical methods like ultra-low energy ion implantation,[21] pulsed laser deposition,[22] magnetron sputtering[23] and plasma processes[24] typically yield AgNPs of higher purity at the expense of the volume (mass production). Furthermore, physical methods generally do not allow a simultaneous precise control over both the size and the surface density of the nanoparticles. Generally, these two factors are interrelated, and an increase in the nanoparticle surface density inevitably leads to structural modifications (size, morphology, *etc.*).[21,24–26] The gas-phase synthesis method, on the other hand, offers the possibility to independently control both the size (through optimization of deposition parameters) and the surface density (by adjusting the deposition time) of the synthesized nanoparticles. However, increasing the deposition time without optimizing the synthesis efficiency, particularly during the nucleation phase of clusters in the gas phase, often results in a waste of time and resources.

The nucleation of metallic clusters in the gas phase has been shown to be highly dependent on the type of gas present in the nucleation chamber. Notably, oxygen has been observed to significantly enhance the nucleation rate, although the underlying mechanism for this effect remains unclear and

[a]*CEMES, CNRS, Université de Toulouse, 29 rue Jeanne Marvig, BP94347, 31055 Toulouse Cedex 04, France. E-mail: benzo@cemes.fr, bonafos@cemes.fr*
[b]*LAPLACE (Laboratoire Plasma et Conversion d'Energie), Université de Toulouse, INPT, CNRS, 118 route de Narbonne, F-31062 Toulouse cedex 9, France*

† Electronic supplementary information (ESI) available. See DOI: https://doi.org/10.1039/d5nr01526j

This journal is © The Royal Society of Chemistry 2025

Open Access Article. Published on 25 June 2025. Downloaded on 2/17/2026 6:44:42 PM.
This article is licensed under a Creative Commons Attribution 3.0 Unported Licence.

debated.[27–30] For example the formation and growth of pure titanium nanoparticles in a low-pressure sputtering plasma are generally deemed unfeasible. However, the introduction of contaminants, such as oxygen or water, is suspected to facilitate nucleation and support nanoparticle growth.[31] Other authors have reported a significant influence of background gas on cluster seed formation in the case of cobalt,[28] copper[27] or tungsten[30] in this type of cluster source. The impact of oxygen on gas-phase elaborated metal nanoparticles extends beyond their size and surface density, also influencing their morphology.[32]

In this study, we explore the influence of various reactive gases commonly used in physical synthesis techniques on the nucleation and growth of AgNPs in the gas phase. In particular, the effect of introducing a small amount of nitrogen (N_2) or oxygen (O_2) into the aggregation chamber on the size and surface density of AgNPs is assessed *in situ* using quadrupole mass spectrometry and *ex situ* by transmission electron microscopy (TEM). Through high-resolution TEM (HRTEM) and energy-dispersive X-ray spectroscopy (EDX) measurements, we demonstrate that the introduction of O_2 into the aggregation chamber does not alter the metallic nature of the synthesized nanoparticles. Finally, supported by *in situ* optical emission spectroscopy measurements, an attempt is made to explain the nucleation mechanisms of AgNPs in the gas phase.

2. Experimental setup

A schematic illustration of the deposition system, from Mantis Deposition Ltd, is presented in Fig. 1a. It consists of a water-cooled Gas Aggregation Source (GAS), a quadrupole mass filter (QMF), and a Ultra High Vacuum deposition chamber (with a base pressure of 5×10^{-10} mbar). Three separate 1″ sputtering targets can be mounted side by side on the same linear translator within the gas aggregation chamber. The aggregation length, defined as the distance between the targets and the exit nozzle, which strongly influences the nanoparticle size by acting on their residence time within the aggregation region, can be adjusted between 0 and 90 mm using a linear translator. Two different gases may be introduced in the vicinity of the metal targets using calibrated mass-flow controllers. The gas inlets are designed so that the flow of the sputtering gas (Ar) is directed from the outside of the targets towards their center, while the flow of the second gas is directed from the center of the targets toward the deposition chamber, along the axis (see Fig. 1b). The gas lines can be pumped out *via* bypass valves for routine cleaning. A differential pressure between the aggregation zone and the deposition chamber drives the NPs toward the substrate holder during the deposition process. Before reaching the sample, the NPs (assumed to be singly charged[33]) travel through an electric field created by four parallel cylindrical rods. An alternative voltage $\Phi_{QMF} = U + V\cos(\omega t)$ is applied to each pair of opposing rods, using opposite polarities. The applied electric field affects the NPs trajectory through the QMF, allowing the transmittance of only NPs of a defined mass. The U/V ratio defines the resolution R_{QMF} of the quadrupole mass filter, *e.g.*, the width of mass band transmitted through the filter. *In situ* NP detection can be performed by measuring the current obtained by a Keithley 6485/E picoammeter connected to a wire mesh grid located after the QMF assembly. In the scanning mode, a frequency sweep of the alternative voltage applied to the rods (in the range 100 Hz–100 kHz) allows for an *in situ* detection of the contri-

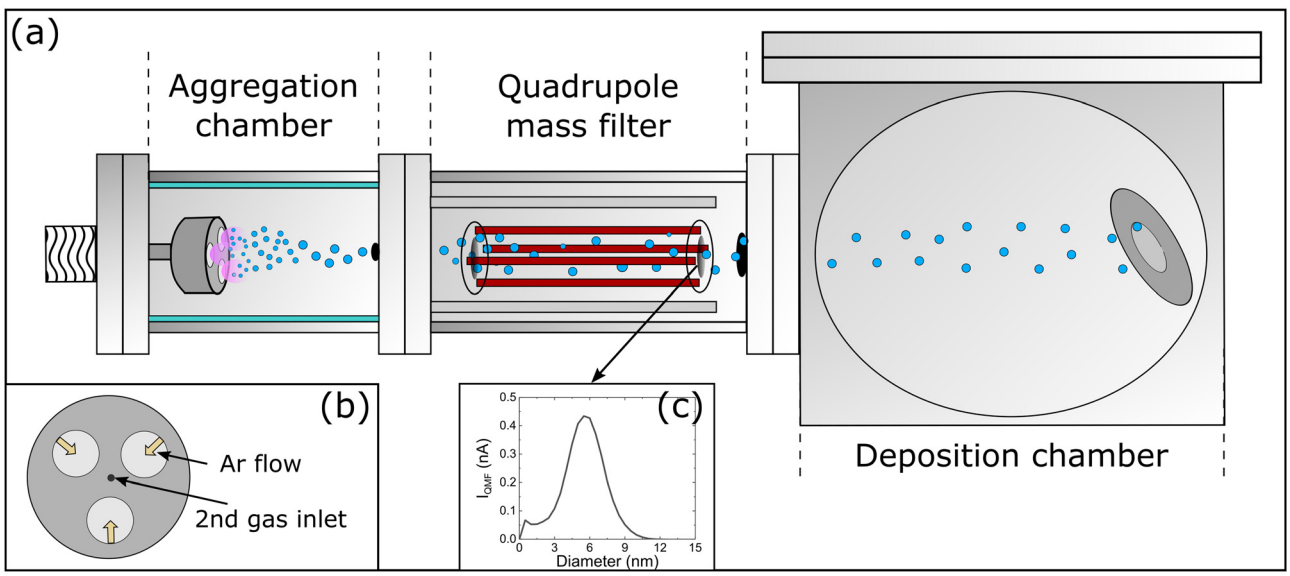

Fig. 1 (a) A schematic diagram of the Nanogen-Trio nanoparticle source from Mantis Deposition, Ltd. It consists of a water-cooled Gas Aggregation chamber, a Quadrupole mass filter (QMF), and an Ultra High Vacuum deposition chamber. (b) The surface of the magnetron head where three targets may be sputtered simultaneously and the direction of the gases introduced into the chamber. (c) A representative example of the QMF current as a function of nanoparticle (NP) diameter under a specific deposition condition.

Open Access Article. Published on 25 June 2025. Downloaded on 2/17/2026 6:44:42 PM. This article is licensed under a Creative Commons Attribution 3.0 Unported Licence.

bution of different NPs sizes. Fig. 1c presents a representative example of the Quadrupole Mass Filter current as a function of nanoparticle diameter. The nanoparticle diameter (d, in nm) is given by the relationship: $d = K \cdot \sqrt[3]{V/(D \cdot f^2)}$, where V [Volts] is the amplitude of the alternating voltage, f [Hz] is its frequency, K [$g^{1/3} \cdot V^{-1/3} \cdot s^{-2/3}$] is a constant determined by geometric parameters, and D [g cm^{-3}] is the density of the deposited material (10.490 g cm^{-3} in the case of silver). Finally, the size-selected NPs are deposited on suitable substrates located on a rotating holder inside the main chamber.

Silver NPs were synthesized using a 99.99% pure silver target purchased from Codex Int. with 1-inch diameter and 3 mm thickness. All experiments on the AgNPs synthesis presented in this work were carried out using a sputtering DC current of 40 mA, applied to a single cathode out of the three available, an Ar (99.9999% purity, AirLiquid Alphagaz 2) flow rate of 80 sccm, an aggregation length of 90 mm and a QMF resolution R_{QMF} = 0.02. The deposition time was set at 20 minutes for all samples. During this time the QMF was used in the scan mode, with a transmitted diameter range between 0.5 and 15 nm. Preliminary studies done by *in situ* QMF current measurements had shown that there were no NPs bigger than 15 nm. The effects of nitrogen were explored using a high-purity N_2 gas (AirLiquid AlphaGaz 2, 99.9999%), while oxygen was introduced either as pure O_2 (AirLiquid AlphaGaz 2, 99.9995%) or as an Ar : O_2 gas mixture (3 mol% O_2, from AirLiquid), the latter allowing for the introduction of very small amounts of oxygen. The gases were introduced into the aggregation zone through a mass flow controller operating in the 0.15–5 sccm range. Ultra-thin carbon coated copper TEM grids were used here as substrates. Bright field (BF) and high-resolution transmission electron microscopy (HRTEM) investigations were carried out using a FEI Tecnai microscope operating at 200 kV and equipped with a spherical aberration (C_s) image corrector. A probe-corrected JEOL ARM200F microscope was used for atomically resolved High-Angle Annular Dark-Field (HAADF) imaging and energy-dispersive X-ray spectroscopy (EDS) analysis in a Scanning Transmission Electron Microscope (STEM) setup. For each sample, AgNPs surface density and size distribution were measured on BF-TEM images, using basic ImageJ software.

The design of Nanogen Trio system, used in this study for AgNPs-synthesis, does not provide access at the level of the cathode (no port is available there), (Fig. 1). This prevents from diagnostic of the plasma. To get insight the elementary processes occurring in the plasma and thus, to assess the impact of small amounts of O_2 on the argon plasma, leading to an increased nucleation of AgNPs we performed a study of the plasma response in a plasma system that also provides AgNPs-synthesis, namely a RF capacitively-coupled axially-asymmetric plasma. Prior to the experiments, we have evaluated the representativity of this asymmetric plasma to the operating conditions of the GAS system. A particular attention was paid to the working pressure that impacts the GAS system in two ways: (1) *via* the permanent magnetic field and (2) *via* the electron-atom elastic collisions occurring in the plasma. The necessary system and plasma parameters to perform the analysis were taken from the literature.[34–38] Detailed description of the procedure is given in the ESI, Section S1.† Briefly, the impact of a permanent magnetic field on the plasma is provided by the Hall plasma parameter for electrons (H_{el}), which gives the number of gyrations that an electron completes around a magnetic field line before undergoing a collision with an atom. Due to the relatively high working pressure in GAS *i.e.*, the high electron-atom elastic collision frequency, the Hall parameter is of only H_{el} = 1.5. It means that the electrons make only 1.5 gyrations around the magnetic field line before colliding with an Ar-atom *i.e.*, the permanent magnetic field has very limited impact on the plasma in GAS. This is the main reason not to use a classical magnetron system for assessment of the role of O_2. It also explains the very large difference between AgNPs synthesized in GAS and in classical magnetron sputtering system, as reported in the literature.[26] Given that the plasma response in GAS is determined by the collisions in the plasma our choice went with a RF capacitively-coupled axially-asymmetric plasma without permanent magnetic field, for which the main plasma parameters (electron number density and electron temperature) are representative of those in GAS. Based on this preliminary assessment, we then investigated the impact of a small amount of O_2, added to the Ar-sputtering gas, on the number density of Ag-species in the gas-phase of a radiofrequency (RF, f = 13.56 MHz) capacitively-coupled axially-asymmetric plasma. This asymmetric plasma process successfully combines sputtering of a metal target and plasma polymerisation. It is sustained with a power of P = 80 W (inducing a self-bias voltage of V_{dc} = −950 V)[24,39] at low gas pressure, $p = 7.21 \times 10^{-2}$ mbar in Ar (AirLiquid AlphaGaz 2, purity 99.9995%). Argon was introduced at a flow rate of 5.25 sccm (standard cubic centimeters per minute at standard temperature and pressure) by a mass-flow controller (Tylan RO-28). The silver target necessary to bear the sputtering was purchased from Codex Int. (purity of 99.99%). The small amount of O_2 (AirLiquid AlphaGaz 2, purity 99.9995%) was mixed to the Ar-gas before being introduced to the plasma. It was varied in the range 0.005–0.1 sccm, thus allowing a fine tuning of the variation of O_2-concentration in the mixture in the range 0–2.0%. The O_2-amount was controlled by a high-precision mass-flow controller (Alicat Scientific, maximum flow rate of 1.0 sccm). Detailed description of the reactor and the plasma process is given elsewhere.[24,39] The plasma emission was collected by an optical fiber and the Optical Emission Spectroscopy (OES) measurements were performed in the spectral range 520–560 nm with a PRINCETON Acton advanced 2500A analyzer.

3. Results and discussion

The effect of two reactive gases (N_2 and O_2) on the nucleation and growth of AgNPs in the gas phase, fabricated using the

 This journal is © The Royal Society of Chemistry 2025

Open Access Article. Published on 25 June 2025. Downloaded on 2/17/2026 6:44:42 PM.
This article is licensed under a Creative Commons Attribution 3.0 Unported Licence.

Mantis system presented in Fig. 1, has been investigated, with particular attention to their influence on nanoparticle size and surface density.

Fig. 2a illustrates the evolution of the QMF spectra as a function of the nitrogen (N_2) concentration, providing qualitative insights into its influence on the size and surface density of nanoparticles. As N_2 is introduced into the aggregation chamber (from 0% to 2.44% and 5.88%), the measured QMF current increases, accompanied by a narrowing of the peak profile and a shift of the maximum towards smaller sizes – from approximately 5.9 ± 2.4 nm for the pure argon sample (black line in Fig. 2a) to 3.1 ± 1.2 nm for the highest N_2 concentration (blue line in Fig. 2a). This trend becomes more pronounced with rising nitrogen concentration, further amplifying the current (see inset of Fig. 2a), refining the peak width, and accentuating the shift towards smaller sizes. To gain deeper quantitative insights into the effects of nitrogen on the size and surface density of AgNPs, TEM analysis are performed.

In Fig. 3a, we show a representative medium magnification bright field image of the AgNPs grown in a pure Ar atmosphere. The mean particle size is around 9.0 ± 1.7 nm and the surface density is less than 1.0×10^9 NPs cm^{-2}. This exceptionally low surface density indicates an extremely limited nucleation under these conditions, suggesting that the pure argon atmosphere does not strongly promote the formation of nucleation sites necessary for a higher surface density of nanoparticles. Fig. 3b and c show similar images of AgNPs, but grown in a mixture of 2 and 5 sccm of nitrogen and 80 sccm of pure argon, corresponding to equivalent nitrogen concentrations of 2.44% and 5.88% respectively. Although the surface density of AgNPs increases up to around 4.5×10^9 NPs cm^{-2} for the higher nitrogen concentration, their diameter is significantly smaller, which indicates a decrease in the total volume of silver aggregated into AgNPs (Fig. 3g). In gas-phase synthesis, nanoparticle growth involves several main steps that take place in the aggregation chamber. Once the material is sputtered into the gas phase, small clusters are formed through homogeneous nucleation (step 1) and grow afterward into stable nanoparticles by condensation (step 2). These nanoparticles then collide and stick together in a process called coagulation or coalescence (step 3), forming aggregates, which are subsequently compacted through sintering (step 4).[40] The observation of a slight increase in nanoparticle surface density, combined with a marked decrease in particle size, suggests that nitrogen does not significantly promote the nucleation of new clusters (step 1). Instead, nitrogen appears to influence the dynamics of particle transport, due to its injection along the axis (Fig. 1b). By increasing the flow rate and promoting faster movement of the nanoparticles, nitrogen reduces their residence time within the aggregation chamber. As a result, there is less time for particles to collide and grow through coagulation or coalescence (step 3). This shortened interaction time limits the growth of nanoparticles, leading to smaller final sizes despite higher particle densities. In this scenario, nitrogen's role is not to directly influence nucleation or growth but to modify the dynamics of particle transport and their residence time in the aggregation chamber.

In the next step, we examined the effect of oxygen on the size and surface density of the deposited AgNPs. Fig. 2b illustrates the evolution of the QMF spectra as a function of O_2 concentration (from 0% to 0.25%, 0.5% and 1%). The observed trend is quite different from what was previously seen for N_2. The measured current increases significantly with the addition of oxygen, and even very low O_2 concentrations (below 0.5%) lead to a pronounced increase in current. Unlike nitrogen, the

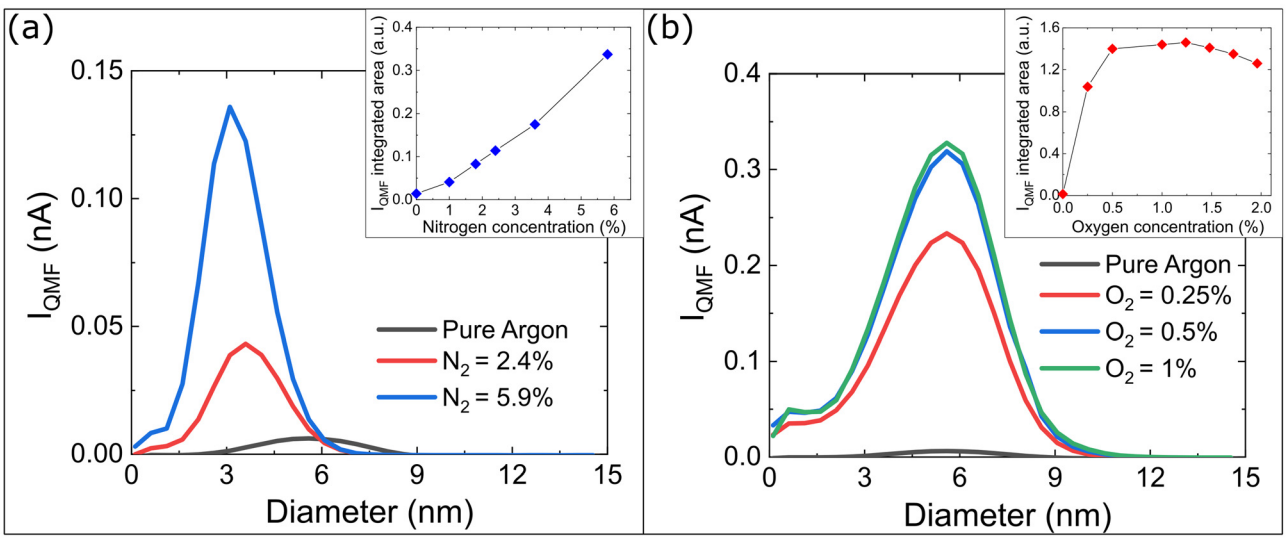

Fig. 2 Evolution of the QMF current as a function of the NPs diameter for different (a) nitrogen (N_2) and (b) oxygen (O_2) concentrations. For clarity, only a selection of representative curves is displayed. The insets show the variation of the integrated area of the measured QMF current as a function of N_2 and O_2 concentrations.

Open Access Article. Published on 25 June 2025. Downloaded on 2/17/2026 6:44:42 PM.
This article is licensed under a Creative Commons Attribution 3.0 Unported Licence.

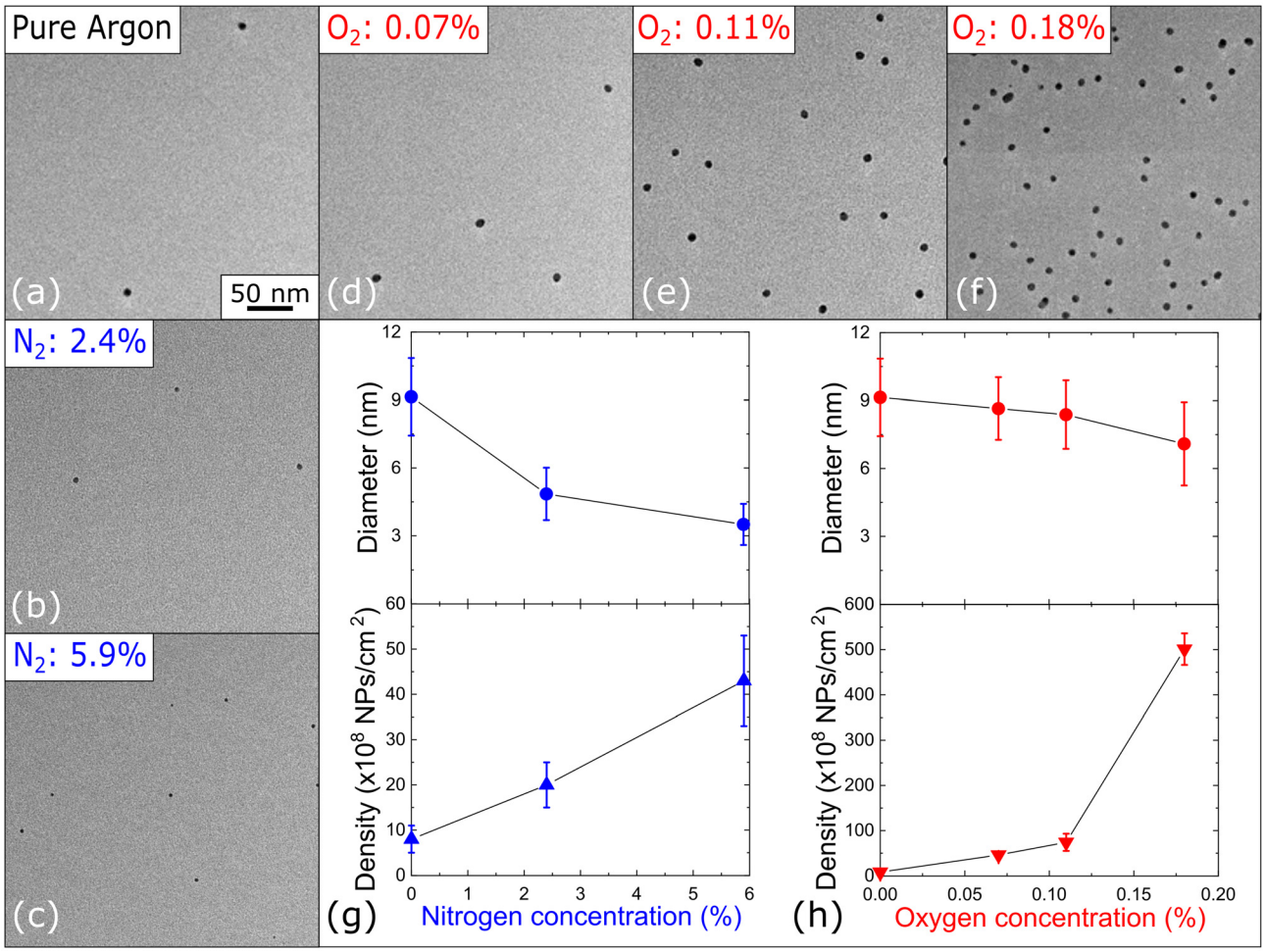

Fig. 3 BF-TEM images of samples synthesized under different gas conditions: (a) using only argon without any additional gas, (b and c) with nitrogen concentrations of 2.44% and 5.88%, respectively, and (d, e and f) with oxygen concentrations of 0.07%, 0.11%, and 0.18%, respectively. Evolution of the mean nanoparticle (NP) diameter and surface density as a function of (g) nitrogen and (h) oxygen concentrations. Error bars for the mean NP size and surface density represent the respective standard deviations.

shift of the maximum towards smaller diameters is much less pronounced in this case. However, a broadening of the curve can be observed as the oxygen concentration increases. Finally, integrating these curves reveals that after a sharp increase at low oxygen concentrations, the signal reaches saturation for concentrations between 0.5% and 1.0% (see inset of Fig. 2b).

Based on the *in situ* QMF current measurements, we conducted a more in-depth investigation of the effect of adding very small amounts of O_2 by introducing trace oxygen into the aggregation chamber using the argon–oxygen gas mixture as a secondary gas. To further examine the structural and morphological evolution of the AgNPs, TEM analysis are performed. Throughout the experiment, the pure argon flow rate was maintained at 80 sccm, while the argon–oxygen flow rate was varied between 2 and 5 sccm, resulting in oxygen concentrations ranging from 0.07% to 0.18% (Fig. 3d–f). In contrast to the effect observed with nitrogen, the introduction of oxygen during deposition significantly increases the surface density of AgNPs; however, its influence on nanoparticle size remains negligible within the examined concentration range. As shown in Fig. 3h, maintaining an oxygen concentration below 0.2% in the mixture leads to an increase in nanoparticle surface density by two orders of magnitude, reaching approximately 5.0×10^{10} NPs cm^{-2}, while the average nanoparticle diameter is only slightly reduced from 9.1 nm to 7.1 nm for a fixed deposition time. This sharp increase in coverage of the substrate by AgNPs reflects a substantial rise in the total volume of silver atoms aggregated into nanoparticles, demonstrating that, unlike nitrogen, oxygen strongly promotes the nucleation process of silver nanoparticles.

An effect of oxygen on the gas-phase nucleation of metallic nanoparticles has already been observed for various metals, including copper,[27] titanium,[27,28] cobalt,[28] palladium[29] and tungsten.[30] In all these cases, adding a small amount of oxygen into the aggregation chamber consistently leads to a higher nucleation rate. Then it reaches a maximum and decreases for higher concentrations. However, the underlying mechanism driving this phenomenon varies depending on the specific metal. The most frequently discussed reasons are oxygen influence on the nucleation process through mecha-

 This journal is © The Royal Society of Chemistry 2025

Open Access Article. Published on 25 June 2025. Downloaded on 2/17/2026 6:44:42 PM.
This article is licensed under a Creative Commons Attribution 3.0 Unported Licence.

nisms such as increasing the sputtering rate or facilitating the formation of metal–oxide seeds by reducing the binding energy of dimers.[28–30]

To determine whether the presence of O_2 affects the structure and composition of the deposited NPs, advanced TEM analysis was conducted by coupling HRTEM observations and STEM-EDX chemical analysis on AgNPs fabricated under conditions of higher oxygen concentration (shown in Fig. 3f). For these measurements, the sample was exposed to air for less than an hour to minimize oxidation of the AgNPs outside the synthesis setup. Fig. 4a shows a representative high-resolution electron microscopy (HRTEM) image of isolated crystalline AgNPs from this sample, viewed along the [110] zone axis. As indicated in the Fast Fourier Transform (FFT) of Fig. 4b, this orientation allows for the measurement of interplanar distances for the {200}, {111}, and {220} families of planes, yielding values of 2.04 Å, 2.36 Å, and 1.44 Å, respectively, which align with those of pure bulk silver. Furthermore, the angles measured between these plane families —54.7° between {200} and {111}, 35.3° between {111} and {220}, and 90° between {200} and {220}—are consistent with those in bulk metallic silver.

These results already indicate that the very small amount of oxygen introduced in the aggregation chamber during the synthesis process is insufficient to promote formation of silver oxide nanoparticles.

To assess the potential presence of oxygen within the AgNPs, atomic resolution elemental cartographies using STEM-EDX were also performed. Fig. 4c shows a representative STEM-HAADF image of an isolated icosahedral nanoparticle, along with the distribution maps of silver (Fig. 4d) and oxygen (Fig. 4e) within this particle, including the superimposition of the two elemental maps (Fig. 4f). The analysis reveals a homogeneous distribution of silver throughout the nanoparticle, with only a negligible amount of oxygen detected. Any observed oxygen signal is likely attributable to background noise rather than indicative of chemical oxidation.

This finding reinforces the idea that, despite the presence of oxygen in the aggregation chamber during the synthesis

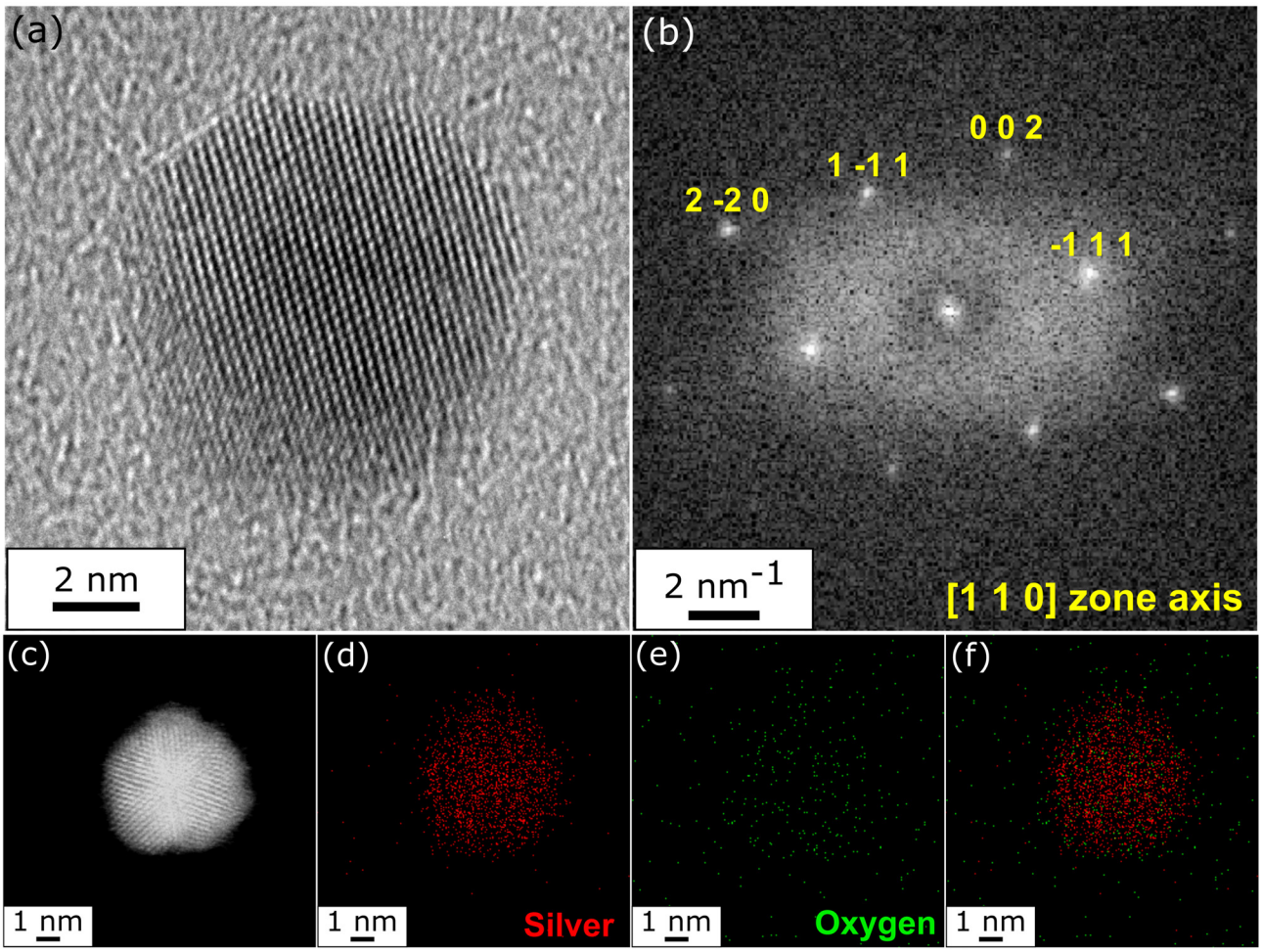

Fig. 4 (a) High-resolution transmission electron microscopy (HRTEM) image of an isolated nanoparticle observed along the [110] zone axis with (b) the corresponding fast Fourier transform (FFT). (c) Scanning transmission electron microscopy-high-angle annular dark field (STEM-HAADF) image of an icosahedral Ag nanoparticle. (d and e) Corresponding energy-dispersive X-ray spectroscopy (EDX) elemental maps for silver and oxygen, respectively. (f) Overlay of the silver and oxygen elemental maps.

Open Access Article. Published on 25 June 2025. Downloaded on 2/17/2026 6:44:42 PM.
This article is licensed under a Creative Commons Attribution 3.0 Unported Licence.

process, the AgNPs predominantly remain in their metallic form, showing no significant signs of oxidation.

These observations are consistent with previous findings indicating that forming Ag_2O during sputtering requires a high oxygen concentration,[41] and that silver oxides are unstable under ultra-high vacuum conditions.[42,43] These results suggest that the observed increase in the nucleation rate is not related to any change in the nature or composition of the nanoparticles. Instead, it implies that the enhancement in nucleation rate is driven by a different mechanism.

In classical nucleation theory, at a fixed temperature, the nucleation rate J, given by $J \propto \exp(-\gamma^3/\ln^2 S)$, is mainly governed by two critical factors: (i) the supersaturation (S) of the metal vapor in the gas phase, expressed as the ratio of the actual vapor pressure to the equilibrium vapor pressure ($S = P/P_{eq}$), and (ii) the surface energy (γ), which denotes the energy needed to form an unit area of the interface between the nucleus and the surrounding vapor. Based on this theory, the presence of oxygen has a dual and contrasting effect on the nucleation of silver. Indeed, in an argon plasma, oxygen slightly increases the vapour pressure of silver,[44] thus decreasing the supersaturation, which negatively impacts the nucleation rate. On the other hand, trace amounts of oxygen (less than 4%O_2) have been shown to significantly influence the deposition of thin silver layers on SiO_2. Acting as a 'surfactant', oxygen alters the surface properties of the film, facilitating percolation at reduced thicknesses.[42] This behavior is attributed to a decrease in surface energy,[42,45] which enhances the nucleation rate despite the lower supersaturation. However, classical nucleation theory exhibits significant limitations when the critical radius of the cluster becomes extremely small, on the scale of just a few atoms, as is the case in our study. Under these conditions, the discrete nature of matter and pronounced surface effects result in substantial deviations from continuum-based predictions, rendering the capillarity approximation inadequate for accurately describing the system and diminishing the very significance of the definition of surface energy. Indeed, in classical nucleation theory, the capillarity approximation assumes that the properties of nanoscale nuclei—such as surface energy—are the same as those of the bulk material. However, at very small sizes (*i.e.*, a few atoms to a few nanometers), this approximation breaks down because surface energy becomes size-dependent and ill-defined. In such cases, atoms at the surface represent a significant fraction of the entire cluster, and the concept of a sharp interface between the "nucleus" and the surrounding vapor becomes ambiguous.

Another possible explanation for the increased surface density of AgNPs observed in our study is the enhancement of active silver nucleation centers in the gas phase in the presence of O_2. Indeed, when active centers are present, the energy barrier for nucleation is significantly reduced, resulting in an overall increase in the nucleation rate. Notably, ions play a crucial role in this process due to their strong ion-dipole and ion-induced dipole interactions, which are well known to lower the thermodynamic barrier to nucleus formation and thereby enhance the nucleation rate.[46,47]

A way to probe the feasibility of this mechanism is to measure the silver components in a plasma process. The impact of a small amount of O_2 on the nucleation of AgNPs has been studied by optical emission spectroscopy (OES) measurements of the atomic species present in the plasma. These measurements were performed in the radiofrequency (RF, f = 13.56 MHz) capacitively-coupled axially-asymmetric plasma system, as described in Section 2. Fig. 5a presents a typical spectrum of the plasma glow emission under the explored operating conditions. Among all spectral lines in the studied spectral range, only two belong to AgI-states, at λ = 520.9 nm and 546.5 nm.[48] The others belong to ArI-states. The methodology of evaluation of the O_2-impact is based on the ratio between the AgI-line at λ = 546.5 nm and an ArI-line at λ = 549.6 nm ($R = I_{Ag(546.5\ nm)}/I_{Ar(549.6\ nm)}$). Working with a line ratio instead of the intensities themselves allows to proceed with arbitrary units. To avoid uncertainties due to small fluctuations in the emission, the line ratio is obtained after integration of the peaks representing the corresponding lines (insert of Fig. 5a). All values of the line ratio presented here are averaged over three independent measurements.

Standard rules apply for the selection of the two spectral lines: (1) spectral lines with close wavelengths, (2) high radiative probability (strong Einstein coefficients of spontaneous emission) and (3) high sensitivity of the spectral lines to variations of the electron number density and electron energy in the plasma. In addition to these criteria, the two selected lines originate from highly excited energetic states, AgI ($4d^{10}5d^2D_{5/2}$, in Paschen's notation, with energy of E_{exc} = 6.05 eV) and ArI ($3s^23p^5$ ($^2P^0_{3/2}$)6d, in Paschen's notation, with energy of E_{exc} = 15.33 eV), close to the ionization energy levels of Ag (E_i = 7.58 eV) and Ar (E_i = 15.76 eV), respectively. This means that the evolution of the intensity of the selected spectral lines can be considered representative of the variations in the number density of the corresponding Ag- and Ar-ions in the plasma.

Fig. 5b shows the variation of the line ratio as a function of the O_2-concentration in the plasma for small amounts of O_2. The difference with a pure Ar-plasma is noticeable. One observes a strong increase of the line ratio for O_2-concentrations up to 0.2%, followed by a maximum for 0.4% of O_2 and a decrease for higher O_2-concentrations to attain a plateau after 1.0% that is kept until the highest studied here O_2-concentration of 2.0%. The variation of the line ratio is mainly sustained by a variation of the intensity of the Ag-line, the intensity of Ar-line remaining almost constant for the entire range of O_2-concentrations. Such behavior indicates that there exist plasma energetic conditions for which the number density of Ag-species increases substantially and these conditions are closely related to the addition of a small amount of O_2, around 0.4%. The clearly pronounced increase in the line ratio, mainly due to the Ag-spectral line, demonstrates that within the range of oxygen concentrations employed in our study, the Ag-ionization is enhanced, eventually reaching saturation at oxygen concentrations around 0.4%.

The probability of ionization of the sputtered Ag-atoms in the plasma is high, especially considering the low energy

 This journal is © The Royal Society of Chemistry 2025

Open Access Article. Published on 25 June 2025. Downloaded on 2/17/2026 6:44:42 PM.
This article is licensed under a Creative Commons Attribution 3.0 Unported Licence.

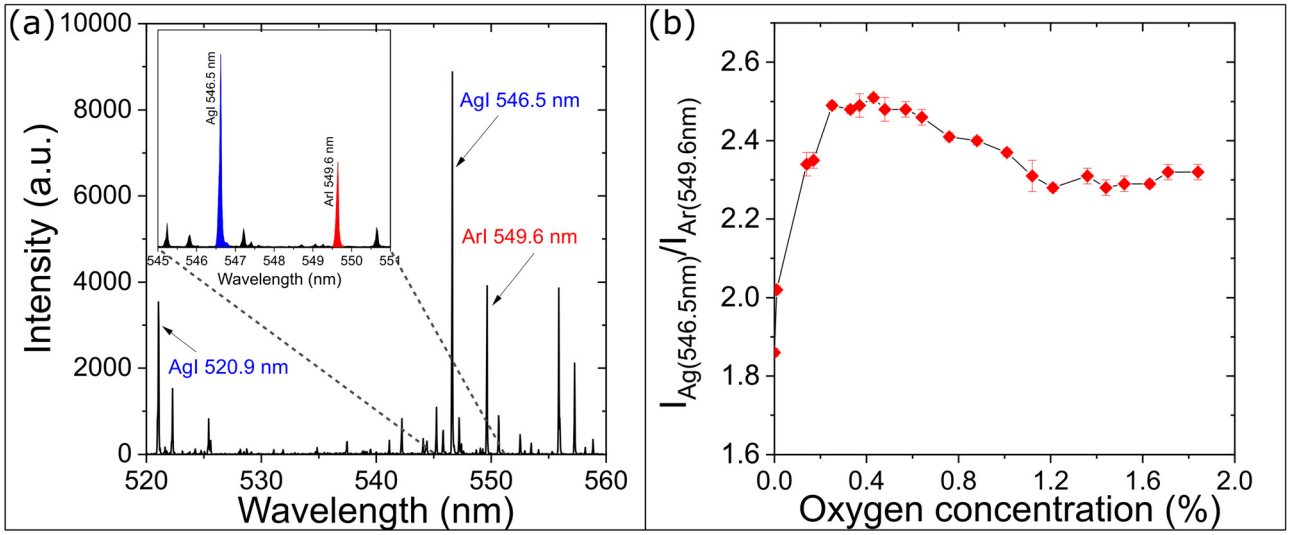

Fig. 5 (a) Typical optical emission spectrum of the plasma. Insert: Zoom in the region of the two selected spectral lines AgI (546.5 nm) and ArI (549.5 nm) (b) variation of the ratio between the two spectral lines ($R = I_{Ag(546.5\ nm)}/I_{Ar(549.6\ nm)}$) as a function of the oxygen concentration in the plasma.

threshold for their ionization (E_i = 7.58 eV), the typical electron number density of $n_e = 10^{10}$ cm^{-3} and the mean electron energy T_e = 2.5 eV in the plasma.[49] It can occur through direct electron impact with the Ag-atoms or Penning ionization *via* the Ar(4s)-excited atoms (E_{exc} = 11.65 eV). Enhancement of the Ag-ionization process due to the presence of O_2 in the plasma is very likely. Addition of a small amount of O_2 (less than 2%) in an Ar-plasma leads to a change in the balance of excited species without significantly changing the plasma maintenance.[50] Indeed, a monotonic decrease of the Ar(4s)-excited atoms is observed after addition of up to 2% O_2 to Ar-plasma due to their strong quenching by O_2 and O. This gain of energy by O_2 and O-states allows additional channels for ionization of the sputtered Ag-atoms. Among the large number of excited states in the O_2-molecule, the Herzberg ($A^3\Sigma_u^+$, $c^1\Sigma_u^-$, $C^3\Delta_u$) and Schuman-Runge ($B^3\Sigma_u^-$) systems require particular attention since their energy range corresponds to the Ag-atom ionization threshold and they may give a great contribution to the processs.[51,52] Despite the limited dissociation of O_2 (less than 15% of O_2 is dissociated), a sufficiently large amount of highly reactive O-atoms is present in the plasma (O-atom number density of no less than 10^{11} cm^{-3}, given the operating gas pressure and gas temperature). This opens another reaction pathway for the creation of Ag-ions. The Penning ionization process would be extremely efficient in this case since the metastable O* (E_{exc} = 9.15 eV) can provide a quasi-resonant transition in the process of Ag-ionization. The obtained results from OES measurements support such kinetic scheme. Simplified potential energy diagrams of Oxygen, Argon and Silver showing the proposed pathways of energy transfer is given in the ESI (Fig. S3†).

This finding supports the conclusion that the observed nucleation phenomenon is ion-induced, amplified by the presence of oxygen. At the concentrations used, oxygen strongly contributes to the ionization of silver, thereby promoting the formation of active nucleation centers.

4. Conclusions

In this work, we successfully synthesized silver nanoparticles in the gas phase and conducted a comprehensive investigation into the influence of reactive gases on their size and surface density. Detailed analysis using advanced transmission electron microscopy, coupled to optical emission spectroscopy of the plasma composition provided critical insights into the underlying gas-phase nucleation mechanisms. Firstly, we demonstrated that nitrogen predominantly serves a passive role, functioning primarily as a carrier gas. Its main contribution lies in facilitating the efficient transport of nanoparticles to the deposition chamber. Then, we demonstrated that oxygen has a much more pronounced impact on the nucleation of AgNPs and that the ion-induced nucleation is a key process. This conclusion is supported by optical emission spectroscopy measurements, which revealed a pronounced enhancement in the concentration of Ag highly excited species, representative of the Ag ions in the plasma with the addition of trace amounts of O_2. These results provide valuable contributions to the understanding of gas-phase nucleation dynamics and the role of reactive species in nanoparticle synthesis.

Author contributions

Salomé Trillot: Conceptualization (equal); data curation (equal); formal analysis (equal); investigation (equal); methodology (equal); validation (equal); visualization (equal); writing

Open Access Article. Published on 25 June 2025. Downloaded on 2/17/2026 6:44:42 PM. This article is licensed under a Creative Commons Attribution 3.0 Unported Licence.

– original draft (equal); writing – review & editing (equal). Patrizio Benzo: Conceptualization (equal); data curation (equal); formal analysis (equal); funding acquisition (equal); investigation (equal); methodology (equal); supervision (equal); validation (equal); visualization (equal); writing – original draft (equal); writing – review & editing (equal). Sophie Barre: Resources (equal); investigation (supporting). Nathalie Tarrat: Conceptualization (supporting); supervision (equal); funding acquisition (equal); writing – review & editing (equal). Magali Benoit: Conceptualization (supporting); supervision (equal); funding acquisition (equal); writing – review & editing (equal). Kremena Makasheva: Conceptualization (equal); data curation (equal); formal analysis (equal); funding acquisition (equal); investigation (equal); methodology (equal); supervision (equal); validation (equal); visualization (equal); writing – original draft (equal); writing – review & editing (equal). Caroline Bonafos: Conceptualization (equal); data curation (equal); formal analysis (equal); funding acquisition (equal); investigation (equal); methodology (equal); project administration (equal); supervision (equal); validation (equal); visualization (equal); writing – original draft (equal); writing – review & editing (equal).

Conflicts of interest

There are no conflicts to declare.

Data availability

The data supporting this article have been included as part of the ESI.†

Acknowledgements

This work was supported by the ANR "BENDIS" (grant no. ANR-21-CE09-0008). We thank Marie-José Casanove from CEMES-CNRS and Yves Huttel from ICMM-CSIC, Madrid for very fruitful discussions. We thank Abdelouahed Lasfar and Christian Pertel from the electronic service of CEMES-CNRS for their contribution to the development of the quadrupole mass filter acquisition system. The authors thank Teresa Hungria from Centre de MicroCaractérisation Raimond Castaing for her assistance with STEM-EDX acquisitions.

References

1 R. Carles, C. Farcau, C. Bonafos, G. Benassayag, M. Bayle, P. Benzo, J. Groenen and A. Zwick, *ACS Nano*, 2011, **5**, 8774–8782.
2 S. A. Maier, P. G. Kik, H. A. Atwater, S. Meltzer, E. Harel, B. E. Koel and A. A. Requicha, *Nat. Mater.*, 2003, **2**, 229–232.
3 G. V. Hartland, *Chem. Rev.*, 2011, **111**, 3858–3887.
4 H. Wang, Y. Wu, H. Zou, Z. Song, Y. Wang, H. Wang and M. Zhou, *ACS Appl. Nano Mater.*, 2023, **6**, 4834–4843.
5 S. Liu, S. Phillips, S. Northrup and N. Levi, *Pharmaceutics*, 2023, **15**, 2466.
6 H. A. Atwater and A. Polman, *Nat. Mater.*, 2010, **9**, 205–213.
7 S. Linic, P. Christopher and D. B. Ingram, *Nat. Mater.*, 2011, **10**, 911–921.
8 G. Prieto, J. Zečević, H. Friedrich, K. P. De Jong and P. E. De Jongh, *Nat. Mater.*, 2013, **12**, 34–39.
9 X. Zhang, Y. L. Chen, R.-S. Liu and D. P. Tsai, *Rep. Prog. Phys.*, 2013, **76**, 046401.
10 G. Cacciato, M. Bayle, A. Pugliara, C. Bonafos, M. Zimbone, V. Privitera, M. G. Grimaldi and R. Carles, *Nanoscale*, 2015, **7**, 13468–13476.
11 S. Chernousova and M. Epple, *Angew. Chem., Int. Ed.*, 2013, **52**, 1636–1653.
12 B. Le Ouay and F. Stellacci, *Nano Today*, 2015, **10**, 339–354.
13 M. Rima, C. Villeneuve-Faure, L. Pilloux, C. Roques, F. El Garah and K. Makasheva, *Biofilm*, 2025, **9**, 100267.
14 R. Foldbjerg and H. Autrup, *Arch. Basic Appl. Med.*, 2013, **1**, 5–15.
15 D. J. Barillo and D. E. Marx, *Burns*, 2014, **40**, S3–S8.
16 E. Körner, M. H. Aguirre, G. Fortunato, A. Ritter, J. Rühe and D. Hegemann, *Plasma Processes Polym.*, 2010, **7**, 619–625.
17 C. Saulou, B. Despax, P. Raynaud, S. Zanna, P. Marcus and M. Mercier-Bonin, *Appl. Surf. Sci.*, 2009, **256**, S35–S39.
18 L. Xu, Y.-Y. Wang, J. Huang, C.-Y. Chen, Z.-X. Wang and H. Xie, *Theranostics*, 2020, **10**, 8996–9031.
19 K. Gudikandula and S. Charya Maringanti, *J. Exp. Nanosci.*, 2016, **11**, 714–721.
20 M. G. Guzmán, J. Dille and S. Godet, *Int. J. Chem. Eng.*, 2009, **2**(3), 104–111.
21 P. Benzo, C. Bonafos, M. Bayle, R. Carles, L. Cattaneo, C. Farcau, G. Benassayag, B. Pécassou and D. Muller, *J. Appl. Phys.*, 2013, **113**, 193505.
22 C. A. Smyth, I. Mirza, J. G. Lunney and E. M. McCabe, *Appl. Surf. Sci.*, 2013, **264**, 31–35.
23 Z. Zhao, J. Sun, S. Xing, D. Liu, G. Zhang, L. Bai and B. Jiang, *J. Alloys Compd.*, 2016, **679**, 88–93.
24 A. Pugliara, C. Bonafos, R. Carles, B. Despax and K. Makasheva, *Mater. Res. Express*, 2015, **2**, 065005.
25 R. Carles, P. Benzo, B. Pécassou and C. Bonafos, *Sci. Rep.*, 2016, **6**, 39164.
26 J. Kratochvíl, A. Kuzminova, O. Kylián and H. Biederman, *Surf. Coat. Technol.*, 2015, **275**, 296–302.
27 A. Marek, J. Valter, S. Kadlec and J. Vyskočil, *Surf. Coat. Technol.*, 2011, **205**, S573–S576.
28 T. Peter, O. Polonskyi, B. Gojdka, A. Mohammad Ahadi, T. Strunskus, V. Zaporojtchenko, H. Biederman and F. Faupel, *J. Appl. Phys.*, 2012, **112**, 114321.
29 W. Chamorro-Coral, A. Caillard, P. Brault, P. Andreazza, C. Coutanceau and S. Baranton, *Plasma Processes Polym.*, 2019, **16**, e1900006.
30 J. Polášek, K. Mašek, A. Marek and J. Vyskočil, *Thin Solid Films*, 2015, **591**, 194–199.
31 R. Gunnarsson, N. Brenning, R. D. Boyd and U. Helmersson, *J. Phys. D: Appl. Phys.*, 2018, **51**, 455201.

 This journal is © The Royal Society of Chemistry 2025

Open Access Article. Published on 25 June 2025. Downloaded on 2/17/2026 6:44:42 PM.
This article is licensed under a Creative Commons Attribution 3.0 Unported Licence.

32 D. Pohl, A. Surrey, L. Schultz and B. Rellinghaus, *Appl. Phys. Lett.*, 2012, **101**, 263105.
33 H. Haberland, M. Karrais, M. Mall and Y. Thurner, *J. Vac. Sci. Technol., A*, 1992, **10**, 3266–3271.
34 K. Makasheva and A. Shivarova, *Phys. Plasmas*, 2001, **8**, 836–845.
35 J. T. Gudmundsson, *Plasma Sources Sci. Technol.*, 2020, **29**, 113001.
36 S. D. Ekpe, F. J. Jimenez, D. J. Field, M. J. Davis and S. K. Dew, *J. Vac. Sci. Technol., A*, 2009, **27**, 1275–1280.
37 J. Kousal, A. Kolpaková, A. Shelemin, P. Kudrna, M. Tichý, O. Kylián, J. Hanuš, A. Choukourov and H. Biederman, *Plasma Sources Sci. Technol.*, 2017, **26**, 105003.
38 T. Sadek, P. Vinchon, A. Durocher-Jean, G. Carnide, M. L. Kahn, R. Clergereaux and L. Stafford, *Atoms*, 2022, **10**, 147.
39 R. Bérard, V. Garofano, C. Joblin, L. Stafford and K. Makasheva, *Front. Nanotechnol.*, 2024, **6**, 1337571.
40 P. Mélinon, *Gas-Phase Synthesis of Nanoparticles*, John Wiley & Sons, Ltd, 2017, pp. 23–38.
41 J. Pierson and C. Rousselot, *Surf. Coat. Technol.*, 2005, **200**, 276–279.
42 R. Zapata, M. Balestrieri, I. Gozhyk, H. Montigaud and R. Lazzari, *ACS Appl. Mater. Interfaces*, 2023, **15**, 36951–36965.
43 T. C. Kaspar, T. Droubay, S. A. Chambers and P. S. Bagus, *J. Phys. Chem. C*, 2010, **114**, 21562–21571.
44 P. G. Fox and R. J. Esdaile, *Acta Metall.*, 1963, **11**, 1363–1365.
45 G. Zhao, E. Jeong, E.-A. Choi, S. M. Yu, J.-S. Bae, S.-G. Lee, S. Z. Han, G.-H. Lee and J. Yun, *Appl. Surf. Sci.*, 2020, **510**, 145515.
46 S. P. Fisenko, D. B. Kane and M. S. El-Shall, *J. Chem. Phys.*, 2005, **123**, 104704.
47 N. T. K. Thanh, N. Maclean and S. Mahiddine, *Chem. Rev.*, 2014, **114**, 7610–7630.
48 *NIST: Atomic Spectra Database Lines Form*, **https://physics.nist.gov/PhysRefData/ASD/lines_form.html**.
49 V. Garofano, R. Bérard, S. Boivin, C. Joblin, K. Makasheva and L. Stafford, *Plasma Sources Sci. Technol.*, 2019, **28**, 055019.
50 S. Rauf and M. J. Kushner, *J. Appl. Phys.*, 1997, **82**, 2805–2813.
51 B. Eliasson and U. Kogelschatz, *J. Phys. B:At., Mol. Opt. Phys.*, 1986, **19**, 1241.
52 J.-P. Booth, A. Chatterjee, O. Guaitella, J. S. Sousa, D. Lopaev, S. Zyryanov, T. Rakhimova, D. Voloshin, Y. Mankelevich, N. de Oliveira and L. Nahon, *Plasma Sources Sci. Technol.*, 2020, **29**, 115009.